

# Chapter

## 13

# Properties and Applications of Thermochromic Vanadium Dioxide Smart Coatings

Mohammed Soltani\*, Anthony B. Kaye<sup>†</sup>

\*RSL-Tech, 9114 Descartes, Montreal, Quebec, Canada

<sup>†</sup>Department of Physics, Texas Tech University, Box 41051, Lubbock, Texas, USA

### 13.1 Introduction and Properties of VO<sub>2</sub>

Since the work of Morin in 1959,<sup>1</sup> the thermochromic material vanadium dioxide (VO<sub>2</sub>) has continued to interest researchers around the world, for both the scientific challenge to understand the complex mechanisms behind its ultrafast phase transition and the development of potential applications using VO<sub>2</sub> for innovative coatings, sensors, and devices.

VO<sub>2</sub> undergoes an ultrafast, reversible, solid-solid semiconductor-to-metallic phase transition (SMT) at the low temperature of  $T_{\text{trans}} \sim 68^\circ\text{C}$ . This phase transition is accompanied by a structural change from a monoclinic crystalline structure (low temperature) to a tetragonal rutile crystalline structure (high-temperature); Figure 13.1 shows the crystalline structures of VO<sub>2</sub> in each of these states.

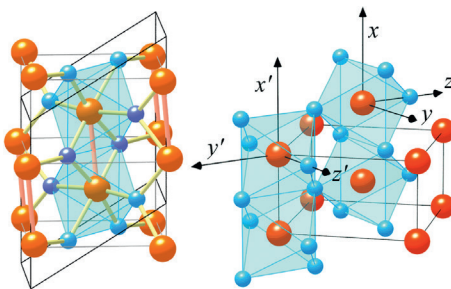


**Figure 13.1** Crystalline structure of  $\text{VO}_2$ : monoclinic (low temperature; left) and tetragonal rutile (high temperature; right) structures are shown with orange/red spheres representing vanadium atoms and blue/purple spheres representing oxygen atoms. Taken from Ref. [2], with permission.

The SMT is also accompanied by a strong change of the electrical and optical properties: the electrical resistivity decreases by almost three orders of magnitude (see Figure 13.8, below), and the material changes from transparent to opaque (with the strongest difference in the large infrared [IR] region of the spectrum, between 1 and  $25\mu\text{m}$ ) as the phase transition occurs. Figure 13.2 shows the IR transmittance of  $\text{VO}_2$ -coated quartz as a function of temperature;  $\text{VO}_2$  is virtually transparent at low temperatures (i.e., in its semiconducting state) and becomes opaque and more reflective at high temperatures. The transmittance in the metallic state drops to zero in the same IR spectral range (Figure 13.2).

Crunteanu et al.<sup>4</sup> shows the temperature dependence of the DC conductivity and the THz transmittance of a 120-nm thick  $\text{VO}_2$  film deposited on c-plane sapphire ( $\text{Al}_2\text{O}_3$ ) substrates; the results are shown in Figure 13.3.

In Figure 13.3, we see that, as the temperature increases, the conductivity also increases, but less of the THz signal is transmitted through the  $\text{VO}_2$  layer.<sup>4</sup> This THz transmissivity variation can be exploited in the fabrication of advanced, tuneable THz systems.

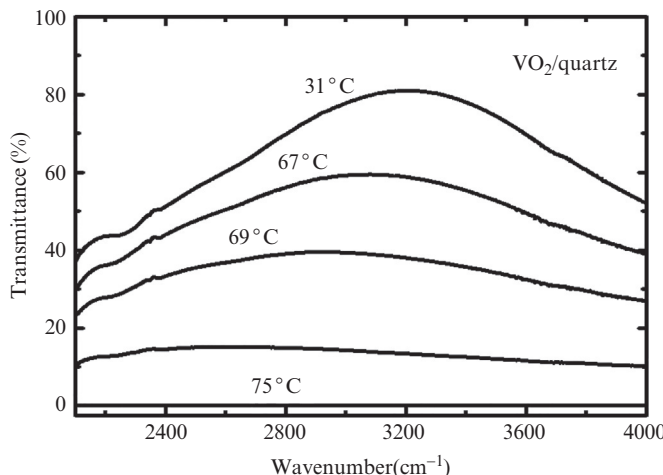


**Figure 13.2** Infrared transmittance during the heating cycle for a  $\text{VO}_2$ -coated quartz substrate. Taken from Ref. [3], with permission.

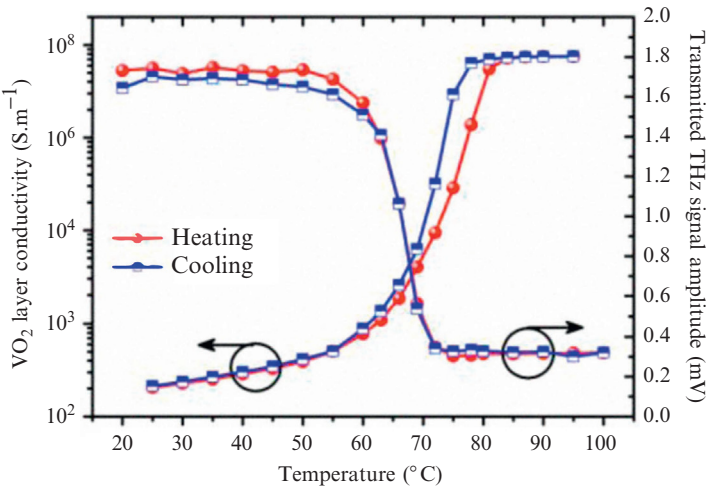


**Figure 13.3** Temperature versus DC conductivity and transmitted THz signal amplitude. Taken from Ref. [4], with permission.

**Figure 13.4** shows a sketch of the valence band diagrams for both the tetragonal rutile (i.e., metallic state; left) and monoclinic ( $M_1$ ) (i.e., semiconducting state; right) phases of  $\text{VO}_2$ . In the tetragonal phase,  $\text{VO}_2$  has one outer  $d$  electron per molecule and the two partially filled  $d_{\parallel}$  and  $d_{\perp}^*$  valence bands overlap. At low temperatures, the vanadium  $\pi^*$  band is above the Fermi energy ( $E_F$ ) and the  $3d$  band is split between one filled  $d_{\parallel}$  band and one empty  $d_{\perp}^*$  band; the energy between these valence bands (i.e., the band gap energy) is 0.67 eV.<sup>5</sup> As a result, when sufficient energy is provided, the charge density increases and  $\text{VO}_2$  switches to its metallic state (see also discussions in Refs. [6,7]).

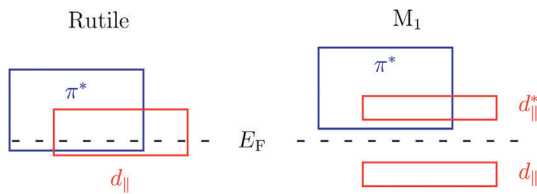


**Figure 13.4** Valence band diagrams for metallic tetragonal (rutile) and semiconducting monoclinic ( $M_1$ ) states of  $\text{VO}_2$ . Taken from Ref. [2], with permission.

### 13.1.1 $\text{VO}_2$ SYNTHESIS METHODS

A variety of methods can be used to synthesize  $\text{VO}_2$ ; these methods include chemical vapor deposition, reactive electron-beam evaporation, reactive magnetron sputtering, pulsed-laser deposition, sol-gel methods, hydrothermal processes, physical vapor transport, and activated reactive evaporation (Table 13.1). In 2008, a comparison of various  $\text{VO}_2$  fabrication methods was published by Nag & Haglund.<sup>55</sup> The

**TABLE 13.1** Methods of VO<sub>2</sub> Synthesis

VO <sub>2</sub> Production Methodology	Example Reference(s)
Chemical vapor deposition	8–12
Reactive electron-beam deposition	13
Reactive magnetron sputtering	14–26
Pulsed laser deposition	27–38
Sol-gel	28,39–48
Hydrothermal process	49
Physical vapor transport	50–53
Activated reactive evaporation	54

thermochromic properties (i.e., transition temperature, switching contrast, hysteresis width) are extremely dependent on the various deposition parameters (e.g., temperature, composition of the deposition atmosphere, and atmospheric pressure) and upon the specific characteristics of the substrate (e.g., material, crystalline structure, and temperature during deposition).<sup>56</sup>

### 13.1.2 SWITCHING TIME OF THE PHASE TRANSITION OF VO<sub>2</sub>

Despite more than 50 years of research, the physical mechanism behind the ultrafast solid-solid SMT of VO<sub>2</sub> is still a topic of controversy. Generally speaking, there are two models that are used to describe the SMT:

- (a) the Peierls model,<sup>6,57–61</sup> in which the SMT is described in terms of interactions between electrons and phonons and is structurally driven, and
- (b) the Mott-Hubbard model,<sup>57,62–65</sup> which describes the SMT in terms of an electron-electron correlation and is therefore charge driven.

This controversy has been discussed in a number of places; excellent discussions can be found in the literature (e.g., Refs. [66–71]), but despite this research, the question remains: Which comes first: the structural change or the electronic transition?

At the same time, a collection of experiments enables us to understand the ultrafast SMT of VO<sub>2</sub>; among other things, the measured transition time is dependent upon:

- the resolution of the experimental setup;
- the properties of the substrate;
- the thickness of the VO<sub>2</sub>, the size and shape of the VO<sub>2</sub> particles, any structural defects present in the sample; and
- the properties of the dopants and/or impurities that are present in the sample.

**Table 13.2** summarizes the measured switching time of VO<sub>2</sub> transitions using femtosecond pump-probe spectroscopy (in transmission and reflection), femtosecond X-ray spectroscopy, four-dimensional imaging, and ultrafast electron microscopy.

**TABLE 13.2** Experimental Switching Time Measurements of the SMT of VO<sub>2</sub>

VO <sub>2</sub> Thickness	Growth Substrate	Measurement Technique	Optical <sup>a</sup> $t_{\text{switch}}$ (fs)	Reference
200 nm	Glass	Femtosecond pump-probe spectroscopy on transmission and reflection modes	500	25
200 nm	Glass	Femtosecond X-ray and pump-probe reflectivity spectroscopy	470	72
50 and 100 nm 50 nm 200 nm	SiO <sub>2</sub> Al <sub>2</sub> O <sub>3</sub> MgO	Pump-probe transient reflectivity	10 <sup>4</sup> -10 <sup>5</sup>	73
25 nm 50 nm 70 nm 90 nm 100 nm 140 nm 160 nm	SiO <sub>2</sub>	Pump-probe transient reflectivity	500 (but slower in deep layers of films thicker than 50 nm)	74
120 nm	BK7 glass	THz pump-probe transmission spectroscopy	6000	75
100 nm	Al <sub>2</sub> O <sub>3</sub>	THz pump-probe transmission spectroscopy	700	76
50-200 nm	Mica	Four-dimensional imaging; ultrafast electron microscopy	3100	48
5 nm single crystal	—	Four-dimensional imaging; ultrafast electron microscopy	307	77
100 nm nanoparticles	Silica	Pump-probe transmission spectroscopy	<120	78

<sup>a</sup>The typical switching time in SMTs that are electrically induced is on the order of one nanosecond slower than that reported in Table 13.1 (see Ref. [79]).

### 13.1.3 EFFECTS OF ATOMIC OXYGEN IRRADIATION ON THE PROPERTIES OF VO<sub>2</sub>

Jiang et al.<sup>80</sup> investigated the effects of atomic oxygen (AO) irradiation on the thermochromic properties of VO<sub>2</sub>-coated aluminum substrates. In this study, a space environment was simulated by irradiating VO<sub>2</sub>/Al with AO doses equivalent to 6 months and 3 years in a typical low Earth orbital environment; results showed that the thermochromic properties of VO<sub>2</sub> were slightly affected by small doses of AO irradiation, but dramatically affected after longer exposures. Scanning electron microscopy (SEM) analysis showed mild erosion of the sample irradiated with high AO doses, and the X-ray photoelectron analysis showed that the oxygen-to-vanadium ratio in the VO<sub>2</sub> sample increased slightly (likely due to the high reactivity of the oxygen ions with the VO<sub>2</sub>).<sup>80</sup> In addition, the IR emittance is temperature dependent; specifically, the IR emittance increased and the  $T_{\text{trans}}$  decreased slightly when VO<sub>2</sub> was irradiated with a high AO dose. Similar increased emittance was observed in the case of high quality of SiO<sub>2</sub> layers, which is currently used as a protective layer in the AO irradiation environment.<sup>80</sup>

The increasing of the IR emittance with the increase in temperature of the VO<sub>2</sub>/Al was exploited in the fabrication of passive smart radiator devices to control the temperature of the spacecraft and then ensure a good operation of the on-board equipment.<sup>80–83</sup>

### 13.1.4 DOPING EFFECTS ON THE PHASE TRANSITION OF VO<sub>2</sub>

The  $T_{\text{trans}}$  of VO<sub>2</sub> is relatively close to room temperature (~68 °C). However, for practical applications,  $T_{\text{trans}}$  must be modified to the specific temperature dictated by the requirements of the device and its operating environment. A wide range of dopants has been used to both increase and decrease the transition temperature of VO<sub>2</sub> (Table 13.3). In the following sections, we describe some of the most interesting results resulting from doping VO<sub>2</sub> with these dopants.

#### 13.1.4.1 Mo dopant and sol-gel VO<sub>2</sub>

Hanlon et al.<sup>111</sup> investigated the effect of Mo doping on the thermochromic properties of VO<sub>2</sub> synthesized on a glass substrate using a sol-gel method. Figure 13.5 compares the electrical conductivity of undoped VO<sub>2</sub> to that of Mo-doped VO<sub>2</sub> films. The conductivity of both undoped and doped VO<sub>2</sub> films increases with temperature. The Mo dopant reduces the hysteresis width and decreases the  $T_{\text{trans}}$ , which reaches 24 °C for 7 at.% of Mo.

#### 13.1.4.2 Co-doping VO<sub>2</sub> with W and F

Burkhardt et al.<sup>86</sup> studied the effects of doping VO<sub>2</sub> with W and F; Figure 13.6 shows the temperature dependence of the transmittance at a wavelength of 2 μm for

**TABLE 13.3** Effects of Dopants on VO<sub>2</sub><sup>6,55</sup>

Dopant	Change in $T_{\text{trans}}$ (°C/at.%)	Sample Reference
F	-35	84–86
Cr	+3	9,87–97
Fe	+3	9,87,93,95–97
Ga	+6.5	98
Al	+9.0	87,93,98,99
Ti	-0.5 to -0.7	88,89,96,97,100
Re	-4	88,101,102
Ir	-4	101
Os	-7	101
Ru	-10	101
Ge	+5	96,98,103,104
Nb	-7.8	40,88,92,93,96,105–109
Ta	-5 to -10	97,108
Mo	-5 to -10	88,105,110–113
W	-23 and -28	3,6,86,88,89,100,105,114–119
Ce	-4.5	120
Au	-6.4	121

undoped, W-doped, and F-doped VO<sub>2</sub> thin films deposited by RF sputtering from a vanadium target in background of O<sub>2</sub>-Ar gas. In addition, Burkhardt et al. found that both dopants decrease  $T_{\text{trans}}$  and narrow the hysteresis at the cost of switching contrast (i.e., variation of the transmittance between the low-temperature and high-temperature states).<sup>86</sup>

#### 13.1.4.3 Ce-doped VO<sub>2</sub>

Recently, Song et al.<sup>120</sup> synthesized Ce-doped VO<sub>2</sub> films on a muscovite substrate using a sol-gel method. The transmittance switching measurements at a wavelength of 2.5 μm showed that Ce decreased  $T_{\text{trans}}$  by about 4.5 °C/at.%. In addition, Song et al.'s results indicate that Ce may be the only VO<sub>2</sub> dopant that reduces the gain size of the VO<sub>2</sub> films (see Figure 13.1 in Song et al.<sup>120</sup>).

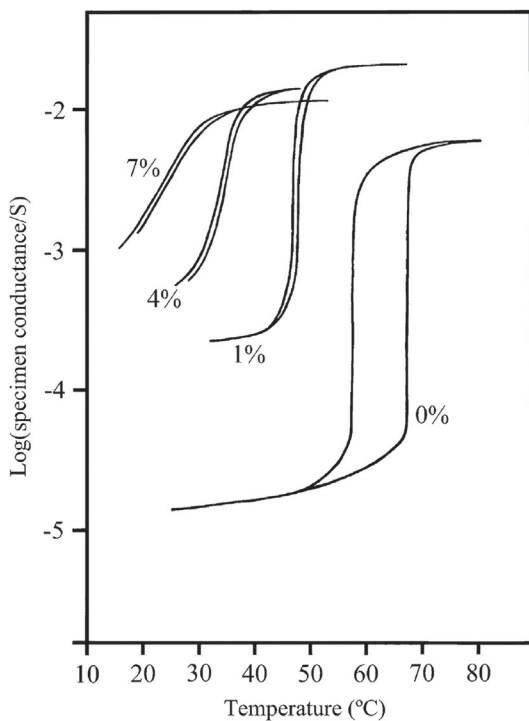


**Figure 13.5** A comparison of the electrical conductivity of undoped, 1 at.%, 4 at.%, and 7 at.% Mo-doped  $\text{VO}_2$  films on glass as a function of temperature. Taken from Ref. [111], with permission.

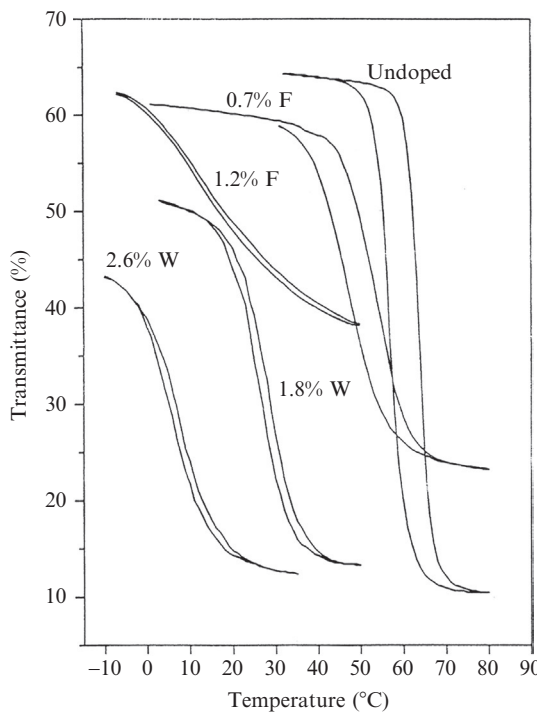


**Figure 13.6** Comparison of the hysteresis loops in transmittance showing switching at  $2\mu\text{m}$  for undoped, W-doped, and F-doped  $\text{VO}_2$  thin films. Taken from Ref. [86], with permission.

### 13.1.4.4 Comparing W-doped and W-Ti Co-doped VO<sub>2</sub>

Soltani et al.<sup>3</sup> studied the effects of doping VO<sub>2</sub> with W and co-doping VO<sub>2</sub> with W and Ti. The results are shown in Figure 13.7, which compares the transmittance at a wavelength of 2.5 μm through both heating and cooling cycles of undoped, W(1.4 at.-%)-doped, and W(1.4 at.-%)-Ti(12 at.-%) co-doped VO<sub>2</sub> thin films on quartz substrates. In this figure, we see that the transmittance drops (i.e., the samples become more opaque) with increasing temperature for undoped and metal-doped VO<sub>2</sub>, but both W and Ti significantly affect the transmittance of the semiconducting state: the transmittance drops from 50% for the undoped film to about 40% for the W-Ti co-doped VO<sub>2</sub> film and to about 30% for W-doped VO<sub>2</sub>. In the metallic state, all of the films are completely opaque. The hysteresis width (about 5 °C) of W-doped VO<sub>2</sub> remains identical to that of undoped VO<sub>2</sub>, but co-doping VO<sub>2</sub> with W and Ti almost completely suppresses the hysteresis—a fact that can be exploited in the fabrication of optical modulators.  $T_{\text{trans}}$  is significantly affected by W doping, dropping to ~36 °C for 1.4 at.% W-doped VO<sub>2</sub> (cf. 68 °C for an undoped VO<sub>2</sub> film of the same thickness) and corresponding to 22.85 °C per at.% W dopant.<sup>3</sup>

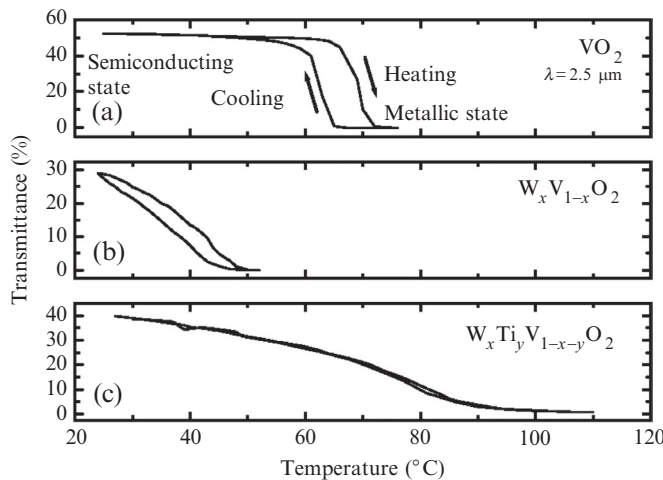


**Figure 13.7** Comparison of the optical hysteresis loops at a wavelength of 2.5 μm obtained from the temperature dependence of the IR transmittance in both heating and cooling cycles of (a) undoped VO<sub>2</sub> (top), (b) W(1.4 at.-%)-doped VO<sub>2</sub> (center), and (c) Ti(12 at.-%)-W(1.4 at.-%) co-doped VO<sub>2</sub> (bottom). Taken from Ref. [3], with permission.

In addition to the optical effects, doping VO<sub>2</sub> with W and Ti also affects electrical resistivity; Figure 13.8 shows the temperature dependence of the electrical resistivity of undoped, W(1.4 at.-%)-doped, and Ti(12 at.-%)-W(1.4 at.-%) co-doped VO<sub>2</sub> thin films. Due to the SMT, the resistivity of all of the samples decreases as the

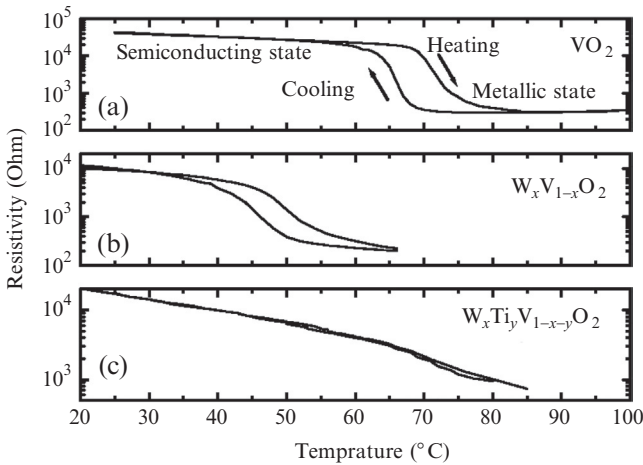


**Figure 13.8** Comparison of the temperature dependence of the electrical resistivity of (a) undoped  $\text{VO}_2$ , (b)  $\text{W}(1.4 \text{ at.}\%)$ -doped  $\text{VO}_2$ , and (c)  $\text{Ti}(12 \text{ at.}\%)$ - $\text{W}(1.4 \text{ at.}\%)$  co-doped  $\text{VO}_2$ . Taken from Ref. [3], with permission.

temperature of the sample increases (i.e., when the sample switches to its metallic state, it is a better conductor). W doping has relatively little effect on the resistivity of the metallic state, but decreases the resistivity of the semiconducting state (i.e., doping with metals makes the semiconducting state more metallic) due to the increase in the number of charge carriers in the film resulting from the presence of the W donor dopant.

Compared to the W-doped  $\text{VO}_2$ , the electrical resistivity of W-Ti co-doped  $\text{VO}_2$  is enhanced in both states. In the W-Ti co-doped film, the Ti concentration (12 at.%) is much higher than that of W dopant (1.4 at.%). As a result, the Ti acceptors compensate for the W donors, causing a decrease in the overall carrier charge and enhancing the resistivity in both states.

The change in resistivity as a function of temperature is exploited in IR bolometers that utilize the change resistivity to measure heating by IR radiation. The principal property that must be maximized in order to achieve maximum sensitivity for IR bolometers is the temperature coefficient of resistance ( $TCR$ ), defined as the slope of the log of electrical resistivity  $R$  of the semiconducting state:

$$TCR = \frac{dR}{RdT} \quad (13.1)$$

The TCR values for  $\text{VO}_2$  ( $-1.76\%/\text{°C}$ ) and W-doped  $\text{VO}_2$  ( $-1.76\%/\text{°C}$ ) are comparable to that of  $\text{VO}_x$  ( $-2\%/\text{°C}$ ) (which is currently used in commercially available uncooled IR micro-bolometers).<sup>122</sup> Raytheon recently patented a neutron detector

system combining a microbolometric sensitive  $\text{VO}_x$  layer with a neutron sensitive reaction layer (e.g.,  $^{10}\text{B}$  or  $^6\text{Li}$ ).<sup>123</sup>

The results of Soltani et al.<sup>3</sup> demonstrate that the Ti-W co-doped  $\text{VO}_2$  results in a much higher TCR ( $-5.12\%/\text{ }^\circ\text{C}$ )—a value comparable to that of a single  $\text{VO}_2$  crystal ( $-6\%/\text{ }^\circ\text{C}$ ). The suppression of both the optical and electrical hysteresis combined with the higher TCR of Ti-W co-doped  $\text{VO}_2$  films will open the way for development of innovative IR sensors based on these characteristics.

## 13.2 Applications

As discussed in Section 13.1.4, the  $T_{\text{trans}}$  of  $\text{VO}_2$  can be tailored to almost any desirable temperature by controlling the concentration levels of dopants. In addition, the SMT of  $\text{VO}_2$  can be initiated by external stimuli such as temperature, pressure, photo-carrier injection, photo-excitation, or an electric field. Indeed, in some cases, these external environments can be constructed in such a way that only a minimum change in the environment is required to initiate the SMT (i.e., a  $\text{VO}_2$  film could be held at a specific voltage potential so that the film required a small amount of thermal energy to initiate the SMT). These characteristics make  $\text{VO}_2$  very attractive for a wide variety of applications. In the following sections, we describe a few of the  $\text{VO}_2$ -enabled applications, including optical and electrical switches, RF-microwave switches, tuneable plasmonic and metamaterial systems, and smart windows.

### 13.2.1 ALL-OPTICAL SWITCHES

All-optical switches are highly desirable for a large number of industrial applications in the communications and computing industries (among others). As we continue to watch Moore's Law being enacted,<sup>124</sup> the issue for integrated circuit manufacturers is no longer the size of the transistors, but the space occupied by interconnects. New paradigms of device performance could become available if we begin to take advantage of the ultrafast switching properties of  $\text{VO}_2$ .

Soltani et al.<sup>37</sup> investigated all-optical switching of undoped and W(1.4 at.%)-doped  $\text{VO}_2$  films using a fiber-fed pump-probe technique in which a continuous wave diode laser ( $\lambda=980\text{ nm}$ ) with controllable power ( $P_{\text{max}}=60\text{ mW}$ ) was used to induce the SMT in the  $\text{VO}_2$  (100–250 nm thick on quartz substrates), while another laser ( $\lambda=1550\text{ nm}$ ) was used to probe the transmittance switching of  $\text{VO}_2$ . Both beams were coupled into a single-mode optical fiber using a "Y" coupler and excited the sample at normal incidence. The transmitted light was collected by a single-mode optical fiber, and the results were recorded as a function of the pump laser power. Figure 13.9 compares the transmittance switching at 1550 nm as a function of increasing pump laser power for  $\text{VO}_2$  and for W-doped  $\text{VO}_2$  films, and shows that

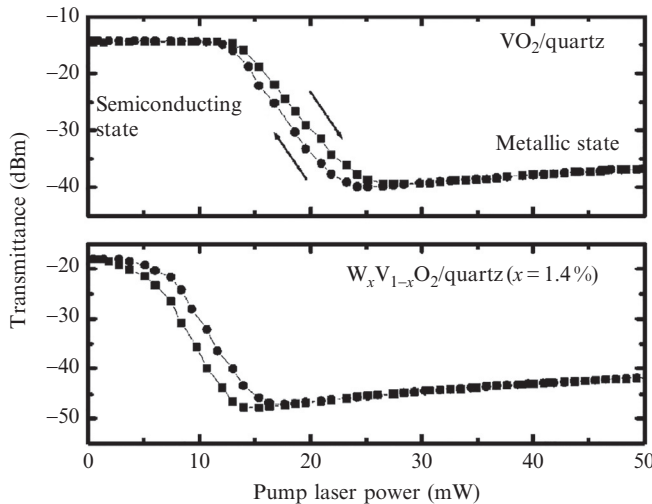


**Figure 13.9** Transmittance switching driven at 980 nm and measured at 1550 nm for  $\text{VO}_2$  and W-doped  $\text{VO}_2$  thin films on quartz substrates. Taken from Ref. [37], with permission.

**TABLE 13.4** Summary of Pump-Probe Results for Undoped and W-Doped  $\text{VO}_2$ <sup>37</sup>

Sample	Pump (980-nm) Power Required for Switching (mW)	Optical Hysteresis Width (mW)	Optical Contrast (dB)
Undoped $\text{VO}_2$	18	1.3	25
W-doped $\text{VO}_2$	10	1.95	28

both films switch from their semiconducting to their metallic states under the photo-excitation by the laser. Table 13.4 summarizes the results.

The switching mechanism in this experiment is due to the change in the band gap energy of  $\text{VO}_2$  from photo-excitation by the pump laser.<sup>125</sup> Since the photon energy used in this experiment ( $h\nu = 1.265 \text{ eV}$ ) is higher than that of the valence band gap energy of  $\text{VO}_2$  ( $0.67 \text{ eV}$ <sup>5</sup>), increasing the pump laser power induces photo-excitation of the electrons from the filled  $d_{\parallel}$  band into the empty  $d_{\parallel}^*$  band. This creation of electron-hole pairs (i.e., excitons) in the  $\text{VO}_2$  film causes overlapping of the  $d_{\parallel}$  and  $d_{\parallel}^*$  valence bands with the one-half filled valence  $d$  band (see Figure 13.4, above). As a result, the charge density increases, and the  $\text{VO}_2$  switches to its metallic state.

Other studies (e.g., Rini et al.<sup>5</sup>) have shown that  $\text{VO}_2$  can be switched well below the band gap energy of  $0.67 \text{ eV}$ . Although the highest contrast switching observed for

$\text{VO}_2$  is in the infrared, other experiments conclude that excitation can be driven by wavelengths in the optical region (even at very low power), although the observed contrast is very small and was assisted by localized surface plasmon resonances (LSPRs) from Au nanoparticles (NPs) (see [Section 13.2.4](#)).<sup>126</sup>

### 13.2.2 ELECTRICAL SWITCHES

---

Soltani et al. excited the  $\text{VO}_2$  SMT by applying up to 20 DC volts and simultaneously measuring the reflectance and transmittance of a  $\text{VO}_2/\text{TiO}_2/\text{ITO}/\text{glass}$  structure at a wavelength of 1550 nm.<sup>125</sup>

In this structure (i.e.,  $\text{VO}_2/\text{TiO}_2/\text{ITO}/\text{glass}$ ),  $\text{TiO}_2$  was used as a buffer layer to improve the crystallinity of the  $\text{VO}_2$ , and ITO was used as transparent electrode. The DC voltage was applied between the ITO (bottom electrode) and the  $\text{VO}_2$  layer (top electrode). The entire structure was probed at incidence angle of 45° by an IR laser beam ( $\lambda=1550\text{ nm}$ ) from a tunable fiber laser source. The reflected and transmitted light was collected by two single-mode optical fibers and recorded by two photodetectors. Figure 7 of Soltani et al.<sup>125</sup> shows results from this experiment in which we see that the transmittance decreases and the reflectance increases with increasing the applied voltage (i.e., the material becomes more opaque and more metallic as the voltage is applied). The extinction ratio between the semiconducting and the metallic states is 12 dB in the transmittance mode and 5 dB in the reflectance mode at a switching voltage of 11.5 V.

The switching mechanism in this case is due to the charge transfer from the  $\text{TiO}_2$  into the  $\text{VO}_2$  layer under voltage.<sup>125</sup> When the applied voltage increases, the carrier charges are injected into  $\text{VO}_2$ , and as a result, the charge density increases and the  $\text{VO}_2$  band gap vanishes (see [Figure 13.4](#), above), resulting in the  $\text{VO}_2$  switching to its metallic state.

### 13.2.3 $\text{VO}_2$ -BASED HYBRID METAMATERIAL DEVICES

---

Metamaterials are engineered materials that are designed to have physical properties that cannot be found in nature and allow the realization of new exciting devices that include (but are not limited to): cloaking, ultrafast optoelectronic switches, high-resolution imaging, transformation optics, radio frequency communications, and millimeter radar. Generally speaking, metamaterial devices consist of a dielectric substrate on which a periodic metallic structure (e.g., sub-wavelength resonator) is placed. The metamaterial's unit cell is designed in such a way that a specific resonant frequency is generated in response to an incident electromagnetic wave. Metamaterial-based systems have been designed to operate in the spectral range from the microwave through the THz to near-visible wavelengths (i.e., a portion of the electromagnetic spectrum ranging from a few mm to 400 nm). Recently, more research efforts have

been concentrated on the realization of tuneable metamaterials with nonlinear properties, and many of these take advantage of VO<sub>2</sub> to accomplish their goals. Incorporating VO<sub>2</sub> enables the devices to be tuneable by modulating the SMT of VO<sub>2</sub> with an external stimulus (e.g., temperature, photo-excitation, and electric fields).

### 13.2.3.1 Tuneable metamaterial devices

Crunteanu et al.<sup>4</sup> exploited the phase transition of VO<sub>2</sub> in the fabrication of thermally tuneable metamaterial devices operating between 0.1 and 1 THz; a sketch of the unit cell and an optical micrograph of their device are shown in the left and right panels of Figure 13.10, respectively.

The VO<sub>2</sub> hybrid metamaterial fabricated by Crunteanu et al. consists of a 500-μm thick c-cut sapphire substrate, a 120-nm thick active layer of VO<sub>2</sub>, and a series of Au (200 nm)/Ti (10 nm) periodic resonator cells assembled using an electron-beam evaporation and lift-off process.<sup>4</sup> This device exploits the thermally controllable THz signal transmitted through the active VO<sub>2</sub> layer.

Crunteanu et al.<sup>4</sup> used THz time-domain spectroscopy to investigate the temperature dependence of the metamaterial devices. The normalized transmitted signals of the incident THz electric field were extracted from the ratio of the Fourier transform time traces of the transmitted THz signals through the device using the c-cut sapphire substrate as a reference; the results are shown in Figure 13.11.

In Figure 13.11, the two different configurations show that the THz transmitted signals are considerably attenuated when the VO<sub>2</sub> active layer switches to its metallic state at 100 °C (red curves exhibiting plateau). In the semiconducting state (at 20 °C; blue curves exhibiting resonant peaks), a resonant frequency of 0.65 THz is observed in the perpendicular configuration (left panel of Figure 13.11); this resonance is red-shifted to 0.45 THz and a second resonant frequency at 0.8 THz (due to the coupling

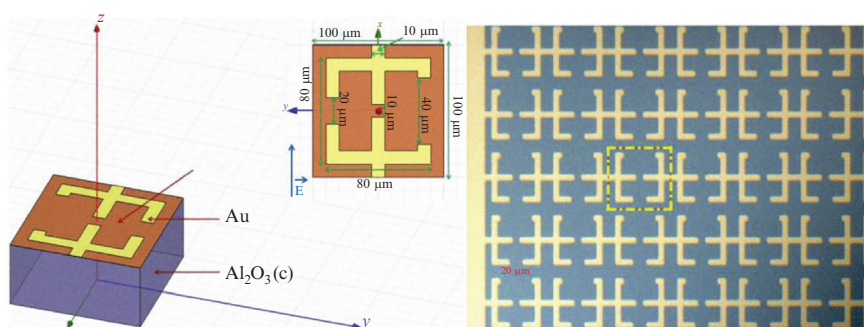


**Figure 13.10** Unit cell of a THz metamaterial (left) and an optical micrograph of the device based upon the sketch. Taken from Ref. [4], with permission.

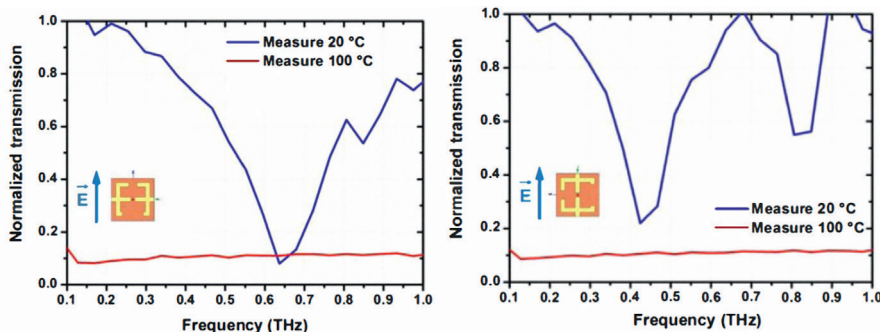


**Figure 13.11** THz transmission through the  $\text{VO}_2$  hybrid metamaterial in the semiconducting (blue) and metallic (red) phases when the incident electric field is perpendicular (left) and parallel (right) to the gap. Taken from Ref. [4], with permission.

of the different branches of the metamaterial's unit cell) is observed in the parallel orientation (right panel of Figure 13.11). These results show that simply rotating the device around the direction of the incident THz electric field can vary the resonant frequency at room temperature.

The fact that we can electronically stimulate the SMT of  $\text{VO}_2$  implies that we can also fabricate  $\text{VO}_2$ -hybrid metamaterial devices that can be electrically tuned. Driscoll et al.<sup>[27]</sup> fabricated such a device by incorporating a patterned single layer of gold split-ring resonator (SRR) arrays onto 90-nm-thick  $\text{VO}_2$  films deposited on a sapphire substrate using a sol-gel method (see panel A of Figure 1 in Driscoll et al.<sup>[27]</sup>). This device exploits the memory effect of the wide hysteresis loop of the SMT of  $\text{VO}_2$  (see panel B of Figure 1 in Driscoll et al.<sup>[27]</sup>): the induced phase transition in  $\text{VO}_2$  layer creates a large change in the permittivity of  $\text{VO}_2$  that then increases the capacitance of the SRR. As a result, the resonant frequency decreases as the temperature increases (see panel C of Figure 1 in Driscoll et al.<sup>[27]</sup>). In the semiconducting state, the resonance frequency is 1.65 THz; this frequency redshifts by ~20% as the temperature increases and induces the phase transition of  $\text{VO}_2$ .

The device's electronic response control was demonstrated by maintaining its temperature at 338.6 K where the hysteresis is more pronounced (see the vertical dotted line in panel B of Figure 1 in Driscoll et al.<sup>[27]</sup>), and by then applying a series of electric pulses to the device. Figure 2 of Driscoll et al.<sup>[27]</sup> shows the effects on the resonant frequency of the device due to the 1-s electric pulses with increasing power. In that figure, we see that the resonant frequency redshifts and the capacitance increases as the power of the electric pulses increases. The frequency remained redshifted even after stopping the electric pulses, thereby demonstrating the persistent change in the  $\text{VO}_2$ -hybrid metamaterial device.

Several groups have modeled these devices using a circuit model, in which each SRR array is modeled by an RLC circuit element with a resonance frequency

$\omega = (LC)^{-1/2}$ .<sup>127</sup> The inductance  $L$  is constant, and the capacitance of the SRR array changes with the frequency  $C/C_0 = (\omega/\omega_0)^2$ . The increase in conductivity introduces a memory capacitance  $C_m$  and a memory resistance  $R_m$ , which reduce the quality factor of the device. The total capacitance  $C_{\text{tot}} = C_0 + C_m$  increases since each electric pulse ( $V_{\text{ext}}$ ) causes the conductivity of the  $\text{VO}_2$  layer to increase.

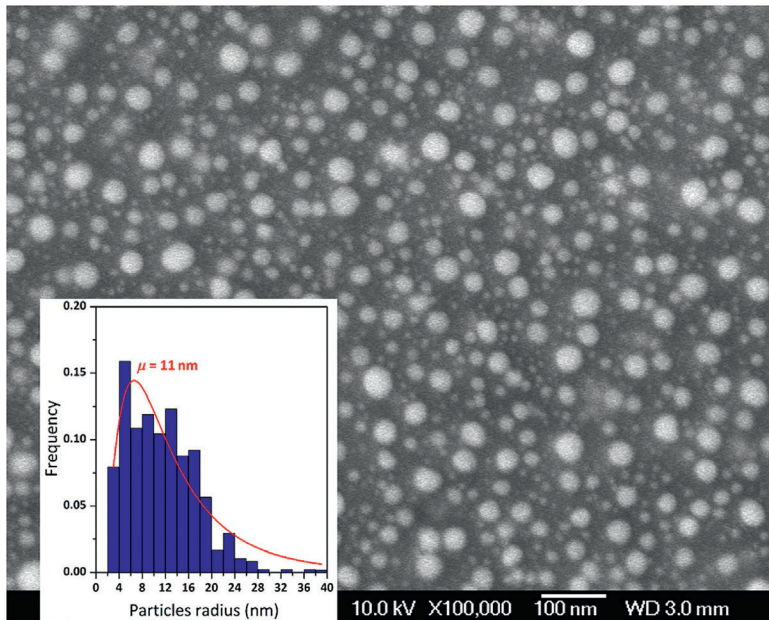


**Figure 13.12** An SEM image of  $\text{VO}_2$ -Au composite material; the inset shows the size distribution of the Au NPs on the surface. Taken from Ref. [128], with permission.

### 13.2.4 $\text{VO}_2$ PLASMONIC DEVICES

Another fascinating application of  $\text{VO}_2$  is the possibility of creating systems in which a LSPR can be generated and tuned by combining  $\text{VO}_2$  with noble metal structures. By selecting the correct material, size, shape, pattern, and surrounding dielectric medium, devices can be finely tuned. Below, we describe three approaches used to fabricate such plasmonic systems: using composites, bilayer structures, and nano-arrays.

#### 13.2.4.1 $\text{VO}_2$ -Au nanoparticle composite

Orlianges et al.<sup>128</sup> investigated the electrical resistivity and optical properties of  $\text{VO}_2$  thin films containing Au nanoparticles (NPs). The  $\text{VO}_2$ -Au nanocomposite had a thickness

of 200 nm that was synthetized by PLD onto c-cut sapphire substrates and alternatively ablating Au and vanadium targets using a KrF laser in an O<sub>2</sub> reactive gas atmosphere at a temperature of 920 K; an image of the resulting material is shown in Figure 13.12.

The temperature dependence of the electrical resistivity measurements showed the normal behavior of the SMT of VO<sub>2</sub>: the resistivity decreased inversely with the temperature for both pure VO<sub>2</sub> films and the VO<sub>2</sub>-Au composite. However, the VO<sub>2</sub>-Au NP composite showed slightly less switching contrast (but within the same order of magnitude of plain VO<sub>2</sub> film) and had a slightly lower  $T_{\text{trans}}$  (341.85 K for VO<sub>2</sub>-Au NPs compared to 345.34 K for the plain VO<sub>2</sub> film). Figure 13.13 shows the transmittance between 300 and 1500 nm for the VO<sub>2</sub>-Au NPs composite, where we see that the transmittance in the NIR decreases with increasing temperature. This behavior is due to the thermally induced increase in free-carrier charge within the VO<sub>2</sub>. The absorption peak near 650 nm is attributed to the LSPR of the Au NPs, and the position of the peak blue-shifts as the temperature increases due to the variation of the dielectric properties of VO<sub>2</sub> at high temperatures (see, e.g., Verleur et al.<sup>[29]</sup>). The transmittance hysteresis loops (see the inset in Figure 13.13) indicate that as the temperature increases, the transmittance at 750 nm increases, but the transmittance at longer wavelengths (e.g., 1550 nm) decreases.

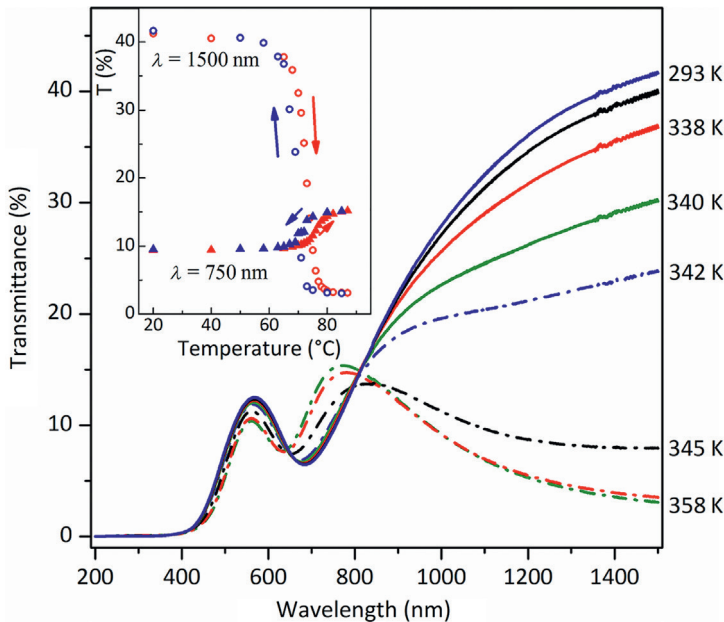


**Figure 13.13** Transmittance spectra of VO<sub>2</sub> film containing Au NPs at selected temperatures during the heating process and thermal hysteresis loops of optical transmittance for 750 and 1500 nm (inset). Taken from Ref. [128], with permission.

### 13.2.4.2 Bilayer structure: Au-nanoparticles/ $\text{VO}_2$ thin films

Xu et al.<sup>[130]</sup> created a bilayered system of Au NPs deposited directly on top of 25 nm of  $\text{VO}_2$  on c-cut sapphire substrates (i.e., Au-NPs/ $\text{VO}_2/\text{Al}_2\text{O}_3$ ). The  $\text{VO}_2$  and Au NPs with equivalent mass thickness ( $d_m = 1, 2, 4$ , and 6 nm) were created using an RF magnetron sputtering process.

The bilayer structure was significantly more opaque in the NIR than the  $\text{VO}_2$  reference material. As expected, both the  $\text{VO}_2$  and bilayer composite samples were transparent in the infrared in the semiconducting state (at 30 °C), but the two samples were quite different once the  $\text{VO}_2$  became metallic (at 80 °C). This difference was caused by the addition of the Au NPs and was very sensitive to the amount of Au in the sample. In addition, as more Au was added, the peak position of the LSPR continuously redshifted (both as a function of the amount of Au and temperature). Figure 13.14 shows the absorption switching of the Au (6 nm)/ $\text{VO}_2$ (25 nm)/sapphire composite with its corresponding LSPR peak position: the redshift of this sample is 200 nm. Note that the LSPR of Au (6 nm)/quartz reference (without  $\text{VO}_2$ ) is unaffected by the temperature increase, showing that this effect must be due to the interaction of the Au with the  $\text{VO}_2$ .

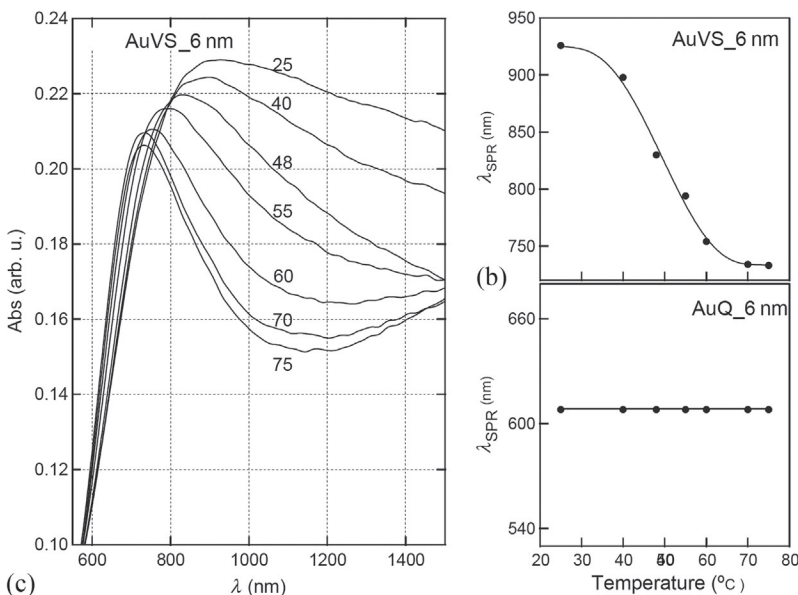


**Figure 13.14** (a) Absorption switching (from 25 up to 75 °C) of Au (6 nm)/ $\text{VO}_2$  (25 nm)/sapphire, (b) the corresponding temperature-dependent of the LSPR wavelength  $\lambda_{\text{LSPR}}$  compared to that of (b) the Au ( $d_m = 6$  nm)/quartz reference without  $\text{VO}_2$ . Taken from Ref. [130], with permission.

### 13.2.4.3 Au::VO<sub>2</sub> nano-arrays

Ferrara et al.<sup>126</sup> compared the optically induced SMT of VO<sub>2</sub> film with that of the plasmonic response of Au::VO<sub>2</sub> nanocomposites. In this case, the nanocomposites consisted of 60 nm of VO<sub>2</sub> on top of 140-nm diameter, 20-nm thick Au arrays. The Au was patterned onto a c-cut sapphire substrate using standard electron-beam lithography techniques, and the VO<sub>2</sub> layer was deposited onto the fabricated Au arrays with PLD. Figure 13.15a shows the SEM image of the fabricated Au array before deposition of the VO<sub>2</sub> layer. Figure 13.15b compares the extinction efficiency of the Au::VO<sub>2</sub> structure when the VO<sub>2</sub> switches from its semiconducting state at 22 °C to its metallic state at 100 °C. Similar to the prior examples, the LSPR redshifts with increasing temperature, but shifts as much as 250 nm using this construction. Figure 13.15c compares the temperature dependence of the absorption at 785 nm for Au::VO<sub>2</sub> structure and VO<sub>2</sub> film. In the semiconducting state, both samples are

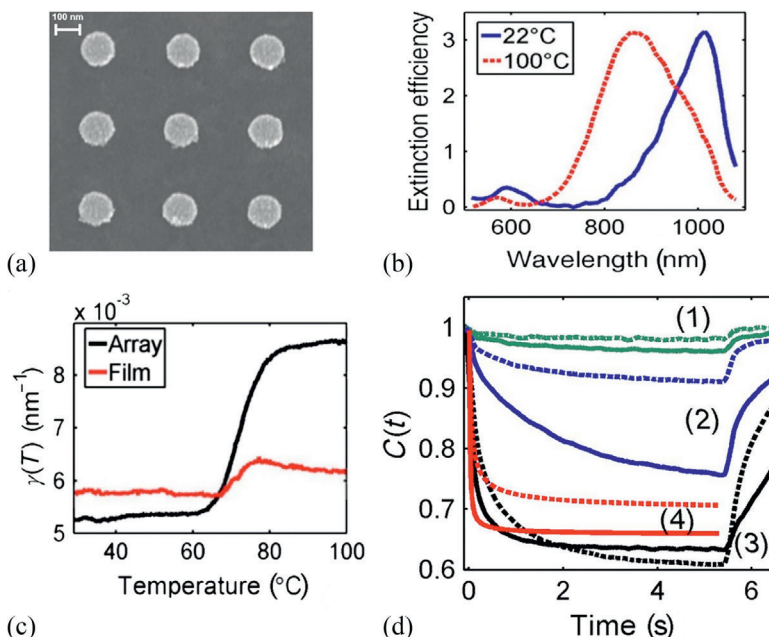


**Figure 13.15** (a) An SEM image of the 140-nm Au array before deposition of the VO<sub>2</sub> film, (b) extinction spectra of 140 nm Au::VO<sub>2</sub> arrays in the semiconducting (blue) and metallic (red) states of VO<sub>2</sub>, (c) absorption coefficient  $\gamma(T)$  taken at  $\lambda = 785 \text{ nm}$  and calculated from transmission measurements, (d) typical  $C(t)$  measurements for the VO<sub>2</sub> film (dashed) and for the Au::VO<sub>2</sub> structure (solid) for 33 (1), 76 (2), and 163  $\text{W cm}^2$  (3); the theoretical prediction from Equation (13.2) for 76  $\text{W cm}^2$  is shown as the pair of curves labeled (4). Taken from Ref. [126], with permission.

relatively transparent, but in the metallic state, the Au::VO<sub>2</sub> is significantly more opaque than plain VO<sub>2</sub> film.

Ferrara et al.<sup>126</sup> also investigated the effects on switching due to optically induced LPSRs using a standard pump-probe experiment. The pump beam (785 nm) with variable intensity  $I$  was used to induce the SMT, while the transmittance of the Au::VO<sub>2</sub> structure was probed by an 18 W/cm<sup>2</sup> diode laser ( $\lambda = 1550$  nm). The temperature of the structure was maintained in the semiconducting state at 55 °C [i.e.,  $T < T_{\text{trans}}(\text{VO}_2)$ ], and for each measurement, the Au::VO<sub>2</sub> nanostructured array was irradiated by the pump beam for 5.3 s. Figure 13.15d shows the contrast of the switching  $C(t)$  (defined as the transmittance at 1550 nm normalized to that of the semiconducting VO<sub>2</sub> for both the Au::VO<sub>2</sub> nanostructured array and the VO<sub>2</sub> film), and as expected, the material becomes opaque when the VO<sub>2</sub> changes phase and the contrast is more dramatic as the laser power is increased.

The Au::VO<sub>2</sub> structure switches to the metallic state faster than plain VO<sub>2</sub> film; at the maximum intensity, the Au::VO<sub>2</sub> structure reaches 85 °C in ~1 s (cf. equilibrium of 5.3 s for the plain VO<sub>2</sub> film). Using first-principles thermodynamics,<sup>126</sup> Ferrara et al. show that the temperature increase  $\Delta T$  of the interface between the substrate and the sample (either plain VO<sub>2</sub> film or a Au::VO<sub>2</sub> nanostructured array) can be described by:

$$\Delta T = \frac{2q\sqrt{\alpha t}}{\kappa} \left[ \frac{1}{\sqrt{\pi}} - i \operatorname{erfc}\left(\frac{a}{2\sqrt{\alpha t}}\right) \right] \quad (13.2)$$

in which  $q = I(1-R)[1-\exp(-\gamma_{\text{eff}}z_0)]$  is the energy absorbed in the sample, and  $\alpha = 5.3 \times 10^{-3}$  cm<sup>2</sup>/s and  $\kappa = 9.6$  mW/(cm °C) are the thermal diffusivity and conductivity of the glass substrate, respectively. In Equation (13.2),  $R$  is the reflectivity at the VO<sub>2</sub>-air interface,  $\gamma_{\text{eff}}$  is the effective laser absorption coefficient, and  $z_0$  is the thickness of the film.

This basic model has a few flaws. It predicts that  $C(t)$  decreases more quickly and  $C_{\max}$  increases more quickly than were experimentally observed. These discrepancies can be explained once we understand that this model overestimates the absorption in the metallic state, which then results in an overestimation of  $C_{\max}$ . The model also ignores the fact that the granular nature of the VO<sub>2</sub> tends to preclude lateral heat diffusion out of the laser focal spot. Despite its shortcomings and relative simplicity, the model does support the main experimental results: the Au::VO<sub>2</sub> reaches a higher VO<sub>2</sub> metallic fraction and a higher  $C_{\max}$  faster than the VO<sub>2</sub> film without the Au nanostructure (Figure 13.15d).

The dynamics of Au::VO<sub>2</sub> structure and VO<sub>2</sub> film were analyzed by fitting  $C_{\max}(I)$  with a three-parameter sigmoid given by:

$$C(I) = 1 - \frac{1 - C_{\text{H}}}{1 + \exp\left(\frac{I - I_{\text{c}}}{I_{\text{w}}}\right)} \quad (13.3)$$

in which  $I_c$  is the critical switching intensity defined at the midpoint of the transition,  $I_w$  is the width of the transition, and  $C_H$  is the high-temperature contrast.<sup>126</sup> The fit to the experimental data (shown in Figure 13.16) indicates that both the  $I_c$  and  $I_w$  decrease by approximately a factor of 1.5 in the case of the Au::VO<sub>2</sub> structure, demonstrating that less pump laser power is required to drive the phase transition of the Au::VO<sub>2</sub> nanostructure than that of plain VO<sub>2</sub>.

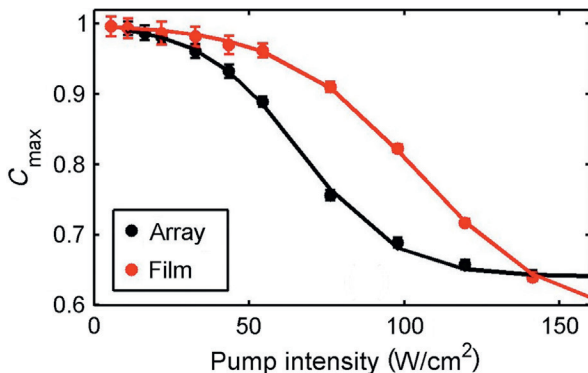


**Figure 13.16** Maximum contrast as a function of the pump intensity for 140 nm Au::VO<sub>2</sub> (black) and VO<sub>2</sub> film (red) at  $t=5.3$  s. Taken from Ref. [126], with permission.

### 13.2.5 VO<sub>2</sub>-BASED RF-MICROWAVE SWITCHES

Dumas-Bouchiat et al.<sup>131</sup> exploited the SMT of VO<sub>2</sub> in order to fabricate RF-microwave switches that operate between 560 MHz and 35 GHz. The design was based on a microwave coplanar waveguide (CPW), and integrated 200 nm of VO<sub>2</sub> as an active layer in two configurations: a shunt configuration (Figure 13.17, top) and a series configuration (Figure 13.17, bottom).

Each device was assembled as follows: (1) the substrate material was selected (either SiO<sub>2</sub>/Si or c-cut sapphire); (2) ~200 nm of evaporated gold was placed onto the substrates; (3) the coplanar waveguides were patterned using lithography and wet etching; (4) a 200-nm thick film of VO<sub>2</sub> was deposited by PLD; and, (5) to minimize propagation losses, the Au lines were thickened by up to ~800 nm.<sup>131</sup> The temperature dependence of the transmittance through the CPW lines was recorded by means of a RF-microwave test bench; Figure 13.18 shows the evolution of the S<sub>21</sub> parameters for the shunt configuration (a; top) and the series configuration (b; bottom) as the VO<sub>2</sub> switches from its semiconducting state at 300 K to its metallic state at 400 K.

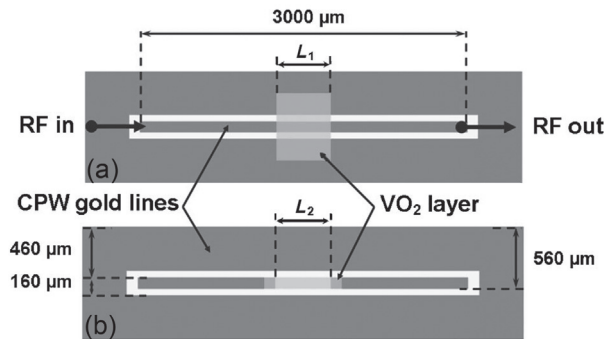


**Figure 13.17** Basic microwave switch design based on  $\text{VO}_2$ . Shunt and series configurations are shown on the top and bottom, respectively. Taken from Ref. [131], with permission.

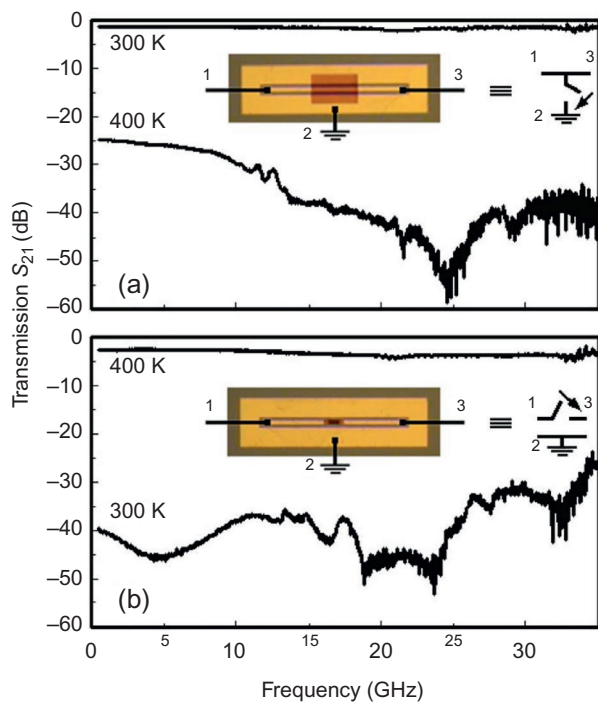


**Figure 13.18** Transmission switching  $S_{21}$  of coplanar waveguide lines deposited on c-cut sapphire in two configurations: (a) shunt (top) and (b) series (bottom). Taken from Ref. [131], with permission.

At 300 K, the shunt switch loses very little signal (about 0.8 dB), but at 400 K, the VO<sub>2</sub> short-circuits the signal to the ground and strongly attenuates the signal (see Figure 13.18a).<sup>131</sup> The series configuration behaves oppositely to the shunt switch: at 300 K, the signal is largely attenuated due to the presence of the VO<sub>2</sub> layer, and at 400 K the signal is transmitted through the metallic state of VO<sub>2</sub> with insertion losses as low as 2.5 dB (see Figure 13.18b).<sup>131</sup>

Despite the differences in electrical resistivity between the VO<sub>2</sub>:Al<sub>2</sub>O<sub>3</sub>(c) and VO<sub>2</sub>:Si/SiO<sub>2</sub> systems, both configurations displayed similar performance, demonstrating that VO<sub>2</sub> is a very promising active material that can be used to fabricate active, high-contrast, high-isolation RF-microwave switches operating over a large frequency range.

### 13.2.6 SMART WINDOWS

---

As discussed in Section 13.1, as a result of the solid-solid phase transition, the IR transmittance of VO<sub>2</sub> changes considerably as a function of temperature, but the visible transmittance remains unchanged. This characteristic can be exploited in “smart windows” applications, in which the external temperature affects the IR thermochromic properties of VO<sub>2</sub> and thereby enables the interior temperature of the building to remain regulated (cooler) with less need for costly air-conditioning systems (for a recent review of this technology, please see the recent review by Kamalisarvestani et al.<sup>132</sup>).

Since the natural  $T_{\text{trans}}$  of VO<sub>2</sub> is higher than that the typical environmental temperature, this application requires the use of doped VO<sub>2</sub> with a tailored  $T_{\text{trans}}$ . Various dopant elements have been used to alter the  $T_{\text{trans}}$  of VO<sub>2</sub> (see Section 13.1.4, above), but these dopants can also degrade the optical and thermochromic properties of VO<sub>2</sub>. Several approaches have been proposed to improve these properties, including those of Li et al.,<sup>133</sup> who proposed using a combination of VO<sub>2</sub> and TiO<sub>2</sub> manufactured as core-shell nanoparticles, which could then be formed into flexible foils and used as a component in these smart windows. The VO<sub>2</sub>/TiO<sub>2</sub> structure integrates the thermochromic properties of VO<sub>2</sub> nanorod cores with the photocatalytic properties of TiO<sub>2</sub> anatase shells. Li et al.<sup>133</sup> also observed that plain VO<sub>2</sub> films are dark yellow (even when quite thin), but the use of VO<sub>2</sub>/TiO<sub>2</sub> core-shell particles to create a film increased the luminous transmittance and changed the color of the films to light blue (see Figure 13.19).

Min et al.<sup>134</sup> developed a VO<sub>2</sub>-based porous structure exhibiting high luminous transmittance and excellent solar modulation efficiency, and recently, Mg-doped VO<sub>2</sub> NPs<sup>135</sup>, F-doped VO<sub>2</sub> NPs,<sup>136</sup> and W-, Mo-, and W-doped VO<sub>2</sub> films were all proposed as potential ways to improve the luminous transmittance of the VO<sub>2</sub>-based smart windows.

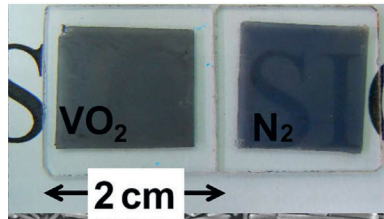


**Figure 13.19** 20-nm  $\text{VO}_2/\text{TiO}_2$  core/shell particle film on glass (left) and 70-nm  $\text{VO}_2/\text{TiO}_2$  core-shell particle film on glass (right). Notice the strong color change from yellow/brown to blue and the transparency difference between the two samples. Taken from Ref. [133], with permission.

### 13.3 Conclusion

In this brief review, we have presented some of the fascinating smart coatings and interesting applications that can only be created using the thermochromic properties and ultrafast SMT of  $\text{VO}_2$ . In addition, it is clear that progress towards commercial “smart windows” continues to be made in leaps and bounds with the improvement of their transmittance in the visible portion of the spectrum and in solar modulation efficiency<sup>[132,137,138]</sup> Finally, we can all look forward to the use of  $\text{VO}_2$  in combination with noble metals in the fabrication of plasmonic- and metamaterial-based devices that can be used in a wide variety of applications including (but not limited to) optical modulators,<sup>[139]</sup> negative capacitors,<sup>[140]</sup> field effect transistors,<sup>[141]</sup> active shutters,<sup>[142]</sup> optical limiting devices,<sup>[143]</sup> sunshields for spacecraft,<sup>[144]</sup> and photonic resonators.<sup>[145]</sup> Many other applications that take advantage of the unique properties of  $\text{VO}_2$  are sure to arise in the near future.

### References

1. Morin F. Oxides which show a metal-to-insulator transition at the Neel temperature. *Phys Rev Lett* 1959;3(1):34–6.
2. Eyert V. The metal insulator transitions of  $\text{VO}_2$ ; a band theoretical approach. *Ann Phys* 2002;11(9):650–704.
3. Soltani M, Chaker M, Haddad E, et al. Effects of Ti–W codoping on the optical and electrical switching of vanadium dioxide thin films grown by a reactive pulsed laser deposition. *Appl Phys Lett* 2004;85(11):1958–60.
4. Crunteanu A, Leroy J, Humbert G, et al. Tunable terahertz metamaterials based on metal-insulator phase transition of  $\text{VO}_2$  layers. In: Microwave symposium digest (MTT), 2012 IEEE MTT-S international; IEEE; 2012. p. 1–3.
5. Rini M, Hao Z, Schoenlein R, et al. Optical switching in  $\text{VO}_2$  films by below-gap excitation. *Appl Phys Lett* 2008;92(18):181904.
6. Goodenough JB. The two components of the crystallographic transition in  $\text{VO}_2$ . *J Solid State Chem* 1971;3:490–500.
7. Goodenough JB. Metallic oxides. *Prog Solid State Chem* 1971;5:145–399.
8. Koide S, Takei H. Epitaxial growth of  $\text{VO}_2$  single crystals and their anisotropic properties in electrical resistivities. *J Physical Soc Japan* 1967;22(3):946–7.

9. Everhart C, MacChesney J. Anisotropy in the electrical resistivity of vanadium dioxide single crystals. *J Appl Phys* 1968;39(6):2872–4.
10. Maruyama T, Ikuta Y. Vanadium dioxide thin films prepared by chemical vapour deposition from vanadium (III) acetylacetone. *J Mater Sci* 1993;28(18):5073–8.
11. Ryabova L, Serbinov I, Darevsky A. Preparation and properties of pyrolysis of vanadium oxide films. *J Electrochem Soc* 1972;119(4):427–9.
12. Ibáñez M, Golmayo D, López C. Vanadium dioxide thermochromic opals grown by chemical vapour deposition. *J Opt A-Pure Appl Opt* 2008;10(12):125202.
13. Marvel R, Appavoo K, Choi B, et al. Electron-beam deposition of vanadium dioxide thin films. *Appl Phys A: Mater Sci Process* 2013;111:975–81.
14. Chain E. Effects of oxygen in ion-beam sputter deposition of vanadium oxide. *J Vac Sci Technol A* 1987;5(4):1836–9.
15. Fuls E, Hensler D, Ross A. Reactively sputtered vanadium dioxide thin films. *Appl Phys Lett* 1967;10(7):199–201.
16. Guinneton F, Sauques L, Valmalette J-C, et al. Optimized infrared switching properties in thermochromic vanadium dioxide thin films: role of deposition process and microstructure. *Thin Solid Films* 2004;446(2):287–95.
17. Rozgonyi G, Hensler D. Structural and electrical properties of vanadium dioxide thin films. *J Vac Sci Technol* 1968;5(6):194–9.
18. Thornton JA. Plasma-assisted deposition processes: theory, mechanisms and applications. *Thin Solid Films* 1983;107(1):3–19.
19. Duchene J, Terraillon M, Pailly M. RF and DC reactive sputtering for crystalline and amorphous VO<sub>2</sub> thin film deposition. *Thin Solid Films* 1972;12(2):231–4.
20. Mahan JE. Physical vapor deposition of thin films, by John E. Mahan. Wiley-VCH; 2000, ISBN: 0-471-33001-9, pp. 336.
21. Wasa K, Kitabake M, Adachi H. Thin films materials technology: sputtering of compound materials. New York: William Andrew, Inc.; 2004.
22. Jin P, Yoshimura K, Tanemura S. Dependence of microstructure and thermochromism on substrate temperature for sputter-deposited VO<sub>2</sub> epitaxial films. *J Vac Sci Technol A* 1997;15(3):1113–7.
23. Rozgonyi G, Polito W. Preparation of thin films of vanadium (di-, sesqui-, and pent-) oxide. *J Electrochem Soc* 1968;115(1):56–7.
24. Lim S, Long J, Xu S, et al. Nanocrystalline vanadium oxide films synthesized by plasma-assisted reactive RF sputtering deposition. *J Phys D Appl Phys* 2007;40(4):1085–90.
25. Becker MF, Buckman AB, Walser RM, et al. Femtosecond laser excitation of the semiconductor-metal phase transition in VO<sub>2</sub>. *Appl Phys Lett* 1994;65(12):1507–9.
26. Chen X, Li J, Lv Q. Thermoelectrical and optical characteristics research on novel nanostructured VO<sub>2</sub> thin film. *Optik Int J Light Electron Opt* 2013;124(15):2041–4.
27. Borek M, Qian F, Nagabushnam V, et al. Pulsed laser deposition of oriented VO<sub>2</sub> thin films on R-cut sapphire substrates. *Appl Phys Lett* 1993;63(24):3288–90.
28. Chae B, Youn D, Kim H, et al. Fabrication and electrical properties of pure VO<sub>2</sub> phase films. *J Korean Phys Soc* 2004;44(4):884–8.
29. Chrisey DB, Hubler GK. Pulsed laser deposition of thin films. In: Chrisey DB, Hubler GK, editors. *Pulsed laser deposition of thin films*. Wiley-VCH; May 2003. p. 648, ISBN: 0-471-59218-8.
30. Eason R. Pulsed laser deposition of thin films: applications-led growth of functional materials. New York: John Wiley & Sons; 2007.
31. Aguadero A, de la Calle C, Pérez-Coll D, et al. Study of the crystal structure, thermal stability and conductivity of Sr(V0.5Mo0.5)O<sub>3</sub>+δ as SOFC material. *Fuel Cells* 2011;11(1):44–50.
32. Kim D, Kwok H. Pulsed laser deposition of VO<sub>2</sub> thin films. *Appl Phys Lett* 1994;65(25):3188–90.

33. Kana Kana JB, Ndjaka JM, Ngom BD, et al. High substrate temperature induced anomalous phase transition temperature shift in sputtered VO<sub>2</sub> thin films. *Opt Mater* 2010;32(7):739–42.
34. Pauli S, Herger R, Willmott P, et al. X-ray diffraction studies of the growth of vanadium dioxide nanoparticles. *J Appl Phys* 2007;102(7):073527.
35. Donev EU, Suh JY, Lopez R, et al. Using a semiconductor-to-metal transition to control optical transmission through subwavelength hole arrays. *Adv Optoelectron* 2008;2008:1–10.
36. Akiyama M, Oki Y, Nagai M. Steam reforming of ethanol over carburized alkali-doped nickel on zirconia and various supports for hydrogen production. *Catal Today* 2012;181(1):4–13.
37. Soltani M, Chaker M, Haddad E, et al. Optical switching of vanadium dioxide thin films deposited by reactive pulsed laser deposition. *J Vac Sci Technol A* 2004;22(3):859–64.
38. Rúa A, Cabrera R, Coy H, et al. Phase transition behavior in microcantilevers coated with M<sub>1</sub>-phase VO<sub>2</sub> and M<sub>2</sub>-phase VO<sub>2</sub>:Cr thin films. *J Appl Phys* 2012;111(10):104502.
39. Beteille F, Livage J. Optical switching in VO<sub>2</sub> thin films. *J Sol-Gel Sci Technol* 1998;13(1–3):915–21.
40. Guzman G, Beteille F, Morineau R, et al. Thermochromic V1-xNb<sub>x</sub>O<sub>2</sub> sol-gel thin films. *Eur J Solid State Inorg Chem* 1995;32(7–8):851–61.
41. Chen H-K, Hung H-C, Yang TC-K, et al. The preparation and characterization of transparent nano-sized thermochromic VO<sub>2</sub>–SiO<sub>2</sub> films from the sol–gel process. *J Non-Cryst Solids* 2004;347(1):138–43.
42. Dachuan Y, Niankan X, Jingyu Z, et al. Vanadium dioxide films with good electrical switching property. *J Phys D Appl Phys* 1996;29(4):1051–7.
43. Guzman G, Beteille F, Morineau R, et al. Electrical switching in VO<sub>2</sub> sol–gel films. *J Mater Chem* 1996;6(3):505–6.
44. Livage J. Sol-gel chemistry and electrochemical properties of vanadium oxide gels. *Solid State Ionics* 1996;86–88:935–42.
45. Appavoo K, Lei DY, Sonnefraud Y, et al. Role of defects in the phase transition of VO<sub>2</sub> nanoparticles probed by plasmon resonance spectroscopy. *Nano Lett* 2012;12(2):780–6.
46. Partlow D, Gurkovich S, Radford K, et al. Switchable vanadium oxide films by a sol-gel process. *J Appl Phys* 1991;70(1):443–52.
47. Wu YF, Fan LL, Chen SM, et al. Spectroscopic analysis of phase constitution of high quality VO<sub>2</sub> thin film prepared by facile sol-gel method. *API Adv* 2013;3(4):042132.
48. Grinolds MS, Lobastov VA, Weissenrieder J, et al. Four-dimensional ultrafast electron microscopy of phase transitions. *Proc Natl Acad Sci* 2006;103(49):18427–31.
49. Popuri SR, Miclau M, Artemenko A, et al. Rapid hydrothermal synthesis of VO<sub>2</sub> (B) and its conversion to thermochromic VO<sub>2</sub> (M<sub>1</sub>). *Inorg Chem* 2013;52(9):4780–5.
50. Guiton BS, Gu Q, Prieto AL, et al. Single-crystalline vanadium dioxide nanowires with rectangular cross sections. *J Am Chem Soc* 2005;127(2):498–9.
51. Bassim ND, Schenck PK, Donev EU, et al. Effects of temperature and oxygen pressure on binary oxide growth using aperture-controlled combinatorial pulsed-laser deposition. *Appl Surf Sci* 2007;254(3):785–8.
52. Wu J, Gu Q, Guiton BS, et al. Strain-induced self organization of metal-insulator domains in single-crystalline VO<sub>2</sub> nanobeams. *Nano Letters* 2006;6(10):2313–7.
53. Tselev A, Luk'yanchuk I, Ivanov I, et al. Symmetry relationship and strain-induced transitions between insulating M<sub>1</sub> and M<sub>2</sub> and metallic R phases of vanadium dioxide. *Nano Letters* 2010;10(11):4409–16.
54. Case FC. Influence of ion beam parameters on the electrical and optical properties of ion assisted reactively evaporated vanadium dioxide thin films. *J Vac Sci Technol A* 1987;5(4):1762–6.
55. Nag J, Haglund Jr. R. Synthesis of vanadium dioxide thin films and nanoparticles. *J Phys Condens Matter* 2008;20(26):264016.
56. Jeong J, Aetukuri N, Graf T, et al. Suppression of metal-insulator transition in VO<sub>2</sub> by electric field-induced oxygen vacancy formation. *Science* 2013;339(6126):1402–5.
57. Zylbersztein A, Mott N. Metal-insulator transition in vanadium dioxide. *Phys Rev B* 1975;11(11):4383.

58. Peierls RE. Quantum theory of solids. Oxford: Oxford University Press; 1955.
59. Wentzcovitch RM, Schulz WW, Allen PB. VO<sub>2</sub>: Peierls or Mott-Hubbard? A view from band theory. *Phys Rev Lett* 1994;72(21):3389–92.
60. Paquet D, Leroux-Hugon P. Electron correlations and electron-lattice interactions in the metal-insulator, ferroelastic transition in VO<sub>2</sub>; a thermodynamical study. *Phys Rev B* 1980;22(11):5284–301.
61. Cavalleri A, Dekorsy T, Chong HH, et al. Evidence for a structurally-driven insulator-to-metal transition in VO<sub>2</sub>; a view from the ultrafast timescale. *Phys Rev B* 2004;70(16):161102.
62. Hubbard J. Electron correlations in narrow energy bands. *Proc R Soc Lond A Math Phys Sci* 1963;276(1365):238–57.
63. Hubbard J. Electron correlations in narrow energy bands. II. The degenerate band case. *Proc R Soc London, Ser A* 1964;277(1369):237–59.
64. Hubbard J. Electron correlations in narrow energy bands. III. An improved solution. *Proc R Soc London, Ser A* 1964;281(1386):401–19.
65. Rice T, Launois H, Pouget J. Comment on “VO<sub>2</sub>: Peierls or mott-hubbard? A view from band theory”. *Phys Rev Lett* 1994;73(22):3042.
66. Cavalleri A, Rini M, Chong H, et al. Band-selective measurements of electron dynamics in VO<sub>2</sub> using femtosecond near-edge X-ray absorption. *Phys Rev Lett* 2005;95(6):067405.
67. Qazilbash MM, Brehm M, Chae B-G, et al. Mott transition in VO<sub>2</sub> revealed by infrared spectroscopy and nano-imaging. *Science* 2007;318(5857):1750–3.
68. Kübler C, Ehrke H, Huber R, et al. Coherent structural dynamics and electronic correlations during an ultrafast insulator-to-metal phase transition in VO<sub>2</sub>. *Phys Rev Lett* 2007;99(11):116401.
69. Biermann S, Poteryaev A, Lichtenstein A, et al. Dynamical singlets and correlation-assisted peierls transition in VO<sub>2</sub>. *Phys Rev Lett* 2005;94(2):026404.
70. Tomczak JM, Biermann S. Effective band structure of correlated materials: the case of VO<sub>2</sub>. *J Phys Condens Matter* 2007;19(36):365206.
71. Haverkort M, Hu Z, Tanaka A, et al. Orbital-assisted metal-insulator transition in VO<sub>2</sub>. *Phys Rev Lett* 2005;95(19):196404.
72. Cavalleri A, Tóth C, Siders C, et al. Femtosecond structural dynamics in VO<sub>2</sub> during an ultrafast solid-solid phase transition. *Phys Rev Lett* 2001;87(23):237401.
73. Lysenko S, Vikhnin V, Zhang G, et al. Insulator-to-metal phase transformation of VO<sub>2</sub> films upon femtosecond laser excitation. *J Electron Mater* 2006;35(10):1866–72.
74. Lysenko S, Rua A, Vikhnin V, et al. Light-induced ultrafast phase transitions in VO<sub>2</sub> thin film. *Appl Surf Sci* 2006;252(15):5512–5.
75. Zhi C, Qi-Ye W, Kai D, et al. Ultrafast and broadband terahertz switching based on photo-induced phase transition in vanadium dioxide films. *Chin Phys Lett* 2013;30(1):017102.
76. Nakajima M, Takubo N, Hiroi Z, et al. Study of photo-induced phenomena in VO<sub>2</sub> by terahertz pump-probe spectroscopy. *J Lumin* 2009;129(12):1802–5.
77. Baum P, Yang D-S, Zewail AH. 4D visualization of transitional structures in phase transformations by electron diffraction. *Science* 2007;318(5851):788–92.
78. Rini M, Cavalleri A, Schoenlein R, et al. Giant, ultrafast optical switching based on an insulator-to-Metaltransition in VO<sub>2</sub> nano-particles: photo-activation of shape-controlledplasmons at 1.55 μm. Berkeley, CA (US): Ernest Orlando Lawrence Berkeley National Laboratory; 2004.
79. Hormoz S, Ramanathan S. Limits on vanadium oxide Mott metal–insulator transition field-effect transistors. *Solid-State Electron* 2010;54(6):654–9.
80. Jiang X, Soltani M, Haddad E, et al. Effects of atomic oxygen on the thermochromic characteristics of VO<sub>2</sub> coating. *J Spacecraft Rockets* 2006;43(3):497–500.
81. [http://www.mpb-space.com/web/smarts\\_structures/radiator.html](http://www.mpb-space.com/web/smarts_structures/radiator.html).
82. Kruzelecky RV, Haddad E, Wong B, et al. Variable emittance thermochromic material and satellite system. *US patent 7761053 B2*; 2010.

83. Soltani M, Chaker M, Haddad E, et al. Thermochromic vanadium dioxide ( $\text{VO}_2$ ) smart coatings for switching applications. In: Chen X, editor. Applied physics in the 21st century. Research Signpost; Kerala, India; 2008. ISBN: 978-81-7895-313-7.
84. Bayard M, Reynolds T, Vlasse M, et al. Preparation and properties of the oxyfluoride systems  $\text{V}_2\text{O}_5\text{F}$  and  $\text{VO}_{2-x}\text{Fx}$ . *J Solid State Chem* 1971;3(4):484–9.
85. Bayard M, Pouchard M, Hagenmuller P, et al. Propriétés magnétiques et électriques de l'oxyfluorure de formule  $\text{VO}_{2-x}\text{Fx}$ . *J Solid State Chem* 1975;12(1):41–50.
86. Burkhardt W, Christmann T, Meyer B, et al. W- and F-doped  $\text{VO}_2$  films studied by photoelectron spectrometry. *Thin Solid Films* 1999;345(2):229–35.
87. Galy J, Casalot A, Darriet J, et al. Some new phases with non-stoichiometric character in  $\text{V}_2\text{O}_5\text{-VO}_2\text{-M}_2\text{O}_3$  systems ( $\text{M} = \text{Al Cr and Fe}$ ). *Bull Soc Chim Fr* 1967;1:227–34.
88. Marinder B-O, Magneli A. Metal-metal bonding in some transition metal dioxides. *Acta Chem Scand* 1957;11(10):1635–40.
89. MacChesney J, Guggenheim H. Growth and electrical properties of vanadium dioxide single crystals containing selected impurity ions. *J Phys Chem Solid* 1969;30(2):225–34.
90. Marezio M, McWhan DB, Remeika J, et al. Structural aspects of the metal-insulator transitions in Cr-Doped  $\text{VO}_2$ . *Phys Rev B* 1972;5(7):2541–51.
91. Pierce J, Goodenough J. Structure of orthorhombic  $\text{V}_{0.95}\text{Cr}_{0.05}\text{O}_2$ . *Phys Rev B* 1972;5(10):4104–11.
92. Pouget J, Lederer P, Schreiber D, et al. Contribution to the study of the metal-insulator transition in the  $\text{V}_{1-x}\text{Nb}_x\text{O}_2$  system—II magnetic properties. *J Phys Chem Solid* 1972;33(10):1961–7.
93. Villeneuve G, Bordet A, Casalot A, et al. Propriétés physiques et structurales de la phase  $\text{Cr}_x\text{V}_{1-x}\text{O}_2$ . *Mater Res Bull* 1971;6(2):119–30.
94. Villeneuve G, Drillon M, Hagenmuller P. Contribution à l'étude structurale des phases  $\text{V}_{1-x}\text{Cr}_x\text{O}_2$ . *Mater Res Bull* 1973;8(9):1111–21.
95. Kosuge K. The phase transition in  $\text{VO}_2$ . *J Physical Soc Japan* 1967;22:551–7.
96. Mitsubishi T. On the phase transformation of  $\text{V}_2\text{O}_5$ . *Jpn J Appl Phys* 1967;6(9):1060–71.
97. Futaki H, Kobayashi K, et al. Thermistor composition containing vanadium dioxide. *U.S. patent 3,402,131*; September 17, 1968.
98. Kitahiro I, Watanabe A. Shift of transition temperature of vanadium dioxide crystals. *Jpn J Appl Phys* 1967;6(8):1023–4.
99. Longo JM, Kierkegaard P. A refinement of the structure of  $\text{V}_2\text{O}_5$ . *Acta Chem Scand* 1970;24(2):420–6.
100. Walter Rüdorff H, Kornelson. *Angew Chem* 1968;7:229.
101. Chamberland BL, Rogers DB. Temperature sensitive conductive metal oxide modified vanadium dioxides. *U.S. patent 3,542,697*; November 24, 1970.
102. Sävborg Ö, Nygren M. Magnetic, electrical, and thermal studies of the  $\text{V}_{1-x}\text{Rex}\text{O}_2$  system with  $0 \leq x \leq 0.15$ . *Phys Status Solidi A* 1977;43(2):645–52.
103. Aoki M, Kobayashi K, Futaki H. Abstract of the fall meeting of the Applied Physical Society of Japan 1965;59. (in Japanese); see also Futaki H, Aoki M. Effects of various doping elements on the transition temperature of vanadium oxide semiconductors. *Jpn J Appl Phys* 1969;8:1008.
104. Neuman C, Lawson A, Brown R. Pressure dependence of the resistance of  $\text{VO}_2$ . *J Chem Phys* 1964;41:1591–5.
105. Batista C, Ribeiro RM, Teixeira V. Synthesis and characterization of  $\text{VO}_2$ -based thermochromic thin films for energy-efficient windows. *Nanoscale Res Lett* 2011;6(1):1–7.
106. Jorgenson G, Lee J. Doped vanadium oxide for optical switching films. *Sol Energy Mater* 1986;14(3):205–14.
107. Rüdorff W, Märklin J. Untersuchungen an ternären Oxiden der Übergangsmetalle. III. Die Rutilphase ( $\text{V}_{1-x}\text{Nb}_x\text{O}_2$ ). *Z Anorg Allg Chem* 1964;334(3–4):142–9.
108. Trarieux H, Bernier JC, Michel A. *Ann Chim* 1969;4:183–94.

109. Villeneuve G, Launay J-C, Hagenmuller P. Proprietes electriques du systeme V<sub>1-x</sub>NbxO<sub>2</sub>. *Solid State Commun* 1974;15(10):1683–7.
110. Kierkegaard P, Axrup S, Isaesson M, et al. Studies on structural relations in crystalline and vitreous compounds. [Stockholm Univ (Sweden) Inst of Inorganic and Physical Chemistry], DTIC Document, DIS No. 31; 1968.
111. Hanlon T, Coath J, Richardson M. Molybdenum-doped vanadium dioxide coatings on glass produced by the aqueous sol-gel method. *Thin Solid Films* 2003;436(2):269–72.
112. Jin P, Tanemura S. V<sub>1-x</sub>Mo<sub>x</sub>O<sub>2</sub> thermochromic films deposited by reactive magnetron sputtering. *Thin Solid Films* 1996;281:239–42.
113. Wu Z, Miyashita A, Yamamoto S, et al. Molybdenum substitutional doping and its effects on phase transition properties in single crystalline vanadium dioxide thin film. *J Appl Phys* 1999;86(9):5311–3.
114. Jin P, Tanemura S. Relationship between transition temperature and x in V<sub>1-x</sub>W<sub>x</sub>O<sub>2</sub> films deposited by dual-target magnetron sputtering. *Jpn J Appl Phys* 1995;34(5A):2459–60.
115. Lee M-H, Kim M-G. RTA and stoichiometry effect on the thermochromism of VO<sub>2</sub> thin films. *Thin Solid Films* 1996;286(1):219–22.
116. Nygren M, Israelsson M. A DTA study of the semiconductor-metallic transition temperature in V<sub>1-x</sub>W<sub>x</sub>O<sub>2</sub>, 0≤x≤0.067. *Mater Res Bull* 1969;4(12):881–6.
117. Reyes J, Sayer M, Chen R. Transport properties of tungsten-doped VO<sub>2</sub>. *Can J Phys* 1976;54(4):408–12.
118. Tang C, Georgopoulos P, Fine M, et al. Local atomic and electronic arrangements in W<sub>x</sub>V<sub>1-x</sub>O<sub>2</sub>. *Phys Rev B* 1985;31(2):1000–11.
119. Tazawa M, Jin P, Tanemura S. Optical constants of V(1-x)W(x)O<sub>2</sub> Films. *Appl Opt* 1998;37(10):1858–61.
120. Song L, Zhang Y, Huang W, et al. Preparation and thermochromic properties of Ce-doped VO<sub>2</sub> films. *Mater Res Bull* 2013;48(6):2268–71.
121. Cavanna E, Segaud J, Livage J. Optical switching of au-doped VO<sub>2</sub> sol-gel films. *Mater Res Bull* 1999;34(2):167–77.
122. Uncooled detectors for thermal imaging cameras. [http://www.flir.com/uploadedfiles/Eurasia/MMC\\_Appl\\_Stories/AS\\_0015\\_EN.pdf](http://www.flir.com/uploadedfiles/Eurasia/MMC_Appl_Stories/AS_0015_EN.pdf).
123. Rhiger DR, Harris B. Neutron detection system. *US Patent 8183537*; 2012.
124. Moore GE. Cramming more components onto integrated circuits. *Electronics* 1965;Volume 38:114–7. See also: Moore GE. Cramming more components onto integrated circuits. *Proc IEEE* 1998; Volume 86(1):82–5.
125. Soltani M, Chaker M, Haddad E, et al. 1 × 2 optical switch devices based on semiconductor-to-metallic phase transition characteristics of VO<sub>2</sub> smart coatings. *Meas Sci Technol* 2006;17(5):1052–6.
126. Ferrara DW, MacQuarrie ER, Nag J, et al. Plasmon-enhanced low-intensity laser switching of gold:vanadium dioxide nanocomposites. *Appl Phys Lett* 2011;98(24):241112.
127. Driscoll T, Kim H-T, Chae B-G, et al. Memory metamaterials. *Science* 2009;325(5947):1518–21.
128. Orlianges JC, Leroy J, Crunteanu A, et al. Electrical and optical properties of vanadium dioxide containing gold nanoparticles deposited by pulsed laser deposition. *Appl Phys Lett* 2012;101(13):133102.
129. Verleur HW, Barker Jr. AS, Berglund CN. Optical properties of VO<sub>2</sub> between 0.25 and 5 eV. *Phys Rev* 1968;172(3):788–98.
130. Xu G, Huang C-M, Tazawa M, et al. Tunable optical properties of nano-Au on vanadium dioxide. *Opt Commun* 2009;282(5):896–902.
131. Dumas-Bouchiat F, Champeaux C, Catherinot A, et al. rf-microwave switches based on reversible semiconductor-metal transition of VO<sub>2</sub> thin films synthesized by pulsed-laser deposition. *Appl Phys Lett* 2007;91(22):223505.

132. Kamalisarvestani M, Saidur R, Mekhilef S, et al. Performance, materials and coating technologies of thermochromic thin films on smart windows. *Renew Sustain Energy Rev* 2013;26:353–64.
133. Li Y, Ji S, Gao Y, et al. Core-shell VO<sub>2</sub>@TiO<sub>2</sub> nanorods that combine thermochromic and photocatalytic properties for application as energy-saving smart coatings. *Sci Rep* 2013;3:1370.
134. Min Zhou JB, Minshan Tao, Rui Zhu, Yingting Lin, Xiaodong Zhang, and Yi Xie. Periodic porous thermochromic VO<sub>2</sub>(M) films with enhanced visible transmittance. *Chem Commun* 2013;49:6021–3.
135. Zhou J, Gao Y, Liu X, et al. Mg-doped VO<sub>2</sub> nanoparticles: hydrothermal synthesis, enhanced visible transmittance and decreased metal–insulator transition temperature. *Phys Chem Chem Phys* 2013;15(20):7505–11.
136. Gao YF, Zhou J, Dai L, et al. F-doped VO<sub>2</sub> nanoparticles for thermochromic energy-saving foils with modified color and enhanced solar-heat shielding ability. *Phys Chem Chem Phys* 2013;15:11723–9.
137. Roberts PMS. Smart window. *Patent application US 20120301642 A1*; 2012.
138. Kim H, Kim Y, Kim KS, et al. Flexible thermochromic films based on hybridized VO<sub>2</sub>/graphene. *ACS Nano* 2013;7(7):5769–76.
139. Jiang L, Carr WN. Design, fabrication and testing of a micromachined thermo-optical light modulator based on a vanadium dioxide array. *J Micromech Microeng* 2004;14(7):833.
140. Soltani M, Chaker M. System and method for generating a negative capacitance. *Patent application US20120286743*; 2012.
141. Byung Gyu CHAE, Hyun Tak KIM, Doo Hyeb YOUN. Field effect transistor using vanadium dioxide layer as channel material and method of manufacturing the field effect transistor. *US patent 6933553 B2*; 2005.
142. Jeffrey De Natale F. Vanadium-dioxide front-end advanced shutter technology. *US patent 8067996 B2*; 2011.
143. Kaye AB, Richard Forsberg HJ. Phase-change materials and optical limiting devices utilizing phase-change materials. *US patent 8259381 B2*; 2012.
144. Soltani M, Chaker M, Haddad E, et al. Thermochromic vanadium dioxide smart coatings grown on Kapton substrates by reactive pulsed laser deposition. *J Vac Sci Technol A* 2006;24(3):612.
145. Bryan L, Jackson LVJ, Zhiyong Li. Photonic device including at least one electromagnetic resonator operably coupled to a state-change material. *US patent 7446929 B1*; 2008.